sensors

MDPI

Communication

A High-Performance UVA Photodetector Based on Polycrystalline Perovskite $MAPbCl_3/TiO_2$ Nanorods Heterojunctions

Yupeng Zhang [1], Yannan Zhai [2], Hui Zhang [2], Zhaoxin Wang [2], Yongfeng Zhang [1], Ruiliang Xu [3,4], Shengping Ruan [1,*] and Jingran Zhou [1,*]

[1] College of Electronic Science & Engineering, Jilin University, 2699 Qianjin Street, Changchun 130012, China; jilinzhangyupeng@sina.com (Y.Z.); 13194369969@163.com (Y.Z.)
[2] Aviation University of Air Force, 7855 Renmin Street, Changchun 130012, China; zhaiyannan@sina.com (Y.Z.); zhanghuirun@163.com (H.Z.); 17704316616@163.com (Z.W.)
[3] State Key Laboratory of High Power Semiconductor Lasers, School of Science, Changchun University of Science and Technology, 7089 Wei-Xing Road, Changchun 130022, China; xurl@cust.edu.cn
[4] Changchun University of Science and Technology Chongqing Research Institute, 618 Liangjiang Road, Chongqing 130022, China
* Correspondence: ruansp@jlu.edu.cn (S.R.); zhoujr@jlu.edu.cn (J.Z.)

Abstract: The application of TiO_2 nanorods in the field of ultraviolet (UV) photodetectors is hindered by a high dark current, which is attributed to crystal surface defects and intrinsic excitation by carrier thermal diffusion. Here, a photodetector based on polycrystalline perovskite $MAPbCl_3/TiO_2$ nanorods heterojunctions has been fabricated to overcome the shortcoming. The structure was composed of horizontal $MAPbCl_3$ polycrystalline and vertically aligned TiO_2 nanorods array. Many localized depletion regions at the $MAPbCl_3/TiO_2$ interface can reduce the dark current. The $TiO_2/MAPbCl_3$ detector shows high performance including a high ratio of light-dark current of about six orders of magnitude, which is much larger than that of the TiO_2 detector. This study indicates the potential in the $TiO_2/MAPbCl_3$ heterojunction to fabricate high-performance UV detectors.

Keywords: polycrystalline perovskite; $MAPbCl_3$; TiO_2 nanorods; heterojunction; dark current; UV photodetector; high performance

Citation: Zhang, Y.; Zhai, Y.; Zhang, H.; Wang, Z.; Zhang, Y.; Xu, R.; Ruan, S.; Zhou, J. A High-Performance UVA Photodetector Based on Polycrystalline Perovskite $MAPbCl_3/TiO_2$ Nanorods Heterojunctions. *Sensors* **2023**, *23*, 6726. https://doi.org/10.3390/s23156726

Academic Editors: Khaled Saoud, Gian Franco Dalla Betta, Sami Rtimi and Fadwa El-Mellouhi

Received: 12 June 2023
Revised: 17 July 2023
Accepted: 25 July 2023
Published: 27 July 2023

1. Introduction

Ultraviolet (UV) photodetectors are widely used in ultraviolet communication, flame detection and biological cell canceration detection [1–4]. Recently, various kinds of structures for UV photodetectors have been fabricated, such as Metal-Semiconductor-Metal (MSM) [5–7], PN junction [8–10], Schottky [11,12] and heterojunction [13,14]. Among the structures above, 1D nanowires and nanorods (TiO_2 [15], ZnO [16], CdS [17], Ga_2O_3 [18] and so on) have drawn considerable attention due to their significant advantages for UV photodetector performance, including the stable spatial distribution of straightforward nanochannels for electron transport and light scattering. However, the detectors often suffer from a large dark current, which increases static power consumption and decreases the ratio of photo-dark current [19,20].

Researchers have found that an advantage of the TiO_2 nanorods array in the UV photodetector is a reduction of the recombination probability of photogenerated electron–hole pairs because of the surface trap states associated with adsorbed O_2 molecules on the surface of TiO_2 nanorods [21]. Hakan Karaagac et al. fabricated a Schottky UV photodetector based on well-aligned TiO_2 nanorod arrays, which exhibits high photosensitivity and excellent spectral selectivity, but the dark current (1.2×10^{-7} A at reverse 1 V) was relatively high [21].

$CH_3NH_3PbCl_3$ ($MAPbCl_3$) absorbs UV light below 400 nm due to its 2.88–3.11 eV bandgap [22–24] and has been applied in UV detection due to its high optical absorption capacity, high carrier mobility, long carrier diffusion length and stability. UV detectors based on $MAPbCl_3$ single crystal show high properties, but the difficult fabrication technique places a restriction on their development in photonic crystal structures [25–27]. Therefore, polycrystalline $MAPbCl_3$ film is preferred to compose the heterojunction. Jialin Yang et al. have successfully studied how a polycrystalline $CH_3NH_3PbCl_3$/ZnO heterojunction improved UV photodetector performance compared to single ZnO, but the dark current remained high [28]. Liu shuo et al. have fabricated a Ga_2O_3/polycrystalline $MAPbCl_3$ UVA photodetector with rapid response and recovery property, which nonetheless had a dark current of 6.8 μA at −1.5 V bias [29].

In this work, a UV photodetector based on polycrystalline perovskite $MAPbCl_3/TiO_2$ nanorods array heterojunction has been successfully prepared. The UV photodetector with many localized depletion regions at the $MAPbCl_3/TiO_2$ interface shows better performance than that of pure TiO_2, with improved dark current, light-dark current ratio and a shorter response time. The results indicate that $MAPbCl_3/TiO_2$ heterojunction is a promising way to improve UV photodetector performance.

2. Materials and Methods

2.1. Preparation of TiO_2 One-Dimensional Nanorods Array Film on FTO

TiO_2 nanorods array film was prepared on the surface of the FTO (fluorine-doped tinoxide) substrate by a low-temperature hydrothermal method. First, FTO substrate (15 Ω per square) was cleaned in acetone, ethanol and deionized water and dried in a nitrogen stream. Subsequently, 10 mL of toluene, 1 mL of tetrabutyltitanate [$Ti(OC_4H_9)_4$], 0.2 mL of titanium tetrachloride and 1 mL hydrochloric acid (37%) were added in a sealed Teflon-lined stainless steel autoclave (23 mL). Then, the substrate was placed in the autoclave, heated at 150 °C for 5 h and air-cooled to room temperature (25 °C). After washing with deionized water, a uniform nanorods array was obtained. The TiO_2 growing system in this experiment is a mixed solution composed of $Ti(OC_4H_9)_4$, $Ti(OH)_4$, HCl and H_2O. $Ti(OC_4H_9)_4$ is a lipid with a boiling point of 310 °C. Due to the effect of HCl, $Ti(OC_4H_9)_4$ does not hydrolyze at room temperature, but it will hydrolyze with water at high temperature and pressure. The polar H_2O was adsorbed on the transparent, which is a conductive glass substrate of FTO with the same polarity. $Ti(OC_4H_9)_4$ then moved to the surface of FTO and hydrolyzed with H_2O to generate $Ti(OH)_4$. Then, $Ti(OH)_4$ combined with each other and underwent a polycondensation reaction to generate TiO_2 and a small amount of H_2O. The TiO_2 nanorods grew firmly on the surface of FTO and the small amount of H_2O generated by the condensation polymerization reaction continued to adsorb on the FTO surface or on the grown hydrophilic TiO_2 layer, like other H_2O. The reaction continued until the TiO_2 nanorods array film generated on FTO [30].

2.2. Preparation of TiO_2 Nanorods/$MAPbCl_3$ Heterojunction on FTO

Polycrystalline $MAPbCl_3$ film was prepared by a one-step spin-coating method with antisolvent-assisting. First, 1 mL dimethyl sulfoxide (DMSO) and 1 mL N, N-Dimethylformamide (DMF) were mixed, and then 0.135 g MACl and 0.566 g $PbCl_2$ were weighed and added to the above solution and stirred for 30 min until the solution became completely transparent to obtain $MAPbCl_3$ precursor solution (1 mol/L) [23]. Then, 75 μL solution was coated on TiO_2 film by rotation for 30 s at 3000 rpm. Next, a drop of toluene was put on the TiO_2 film and spun for 20 s. Finally, it was dried at 80 °C for 5 h. Finally, two Ag paste pads were deposited directly on the film and FTO, respectively, to make a Schottky photodiode UV detector. The active area of the electrode is about 0.25 mm^2.

2.3. Material Characterization and Device Measurement

The morphology of the prepared films was characterized by a scanning electron microscope (SEM JEOS JSM-6700F). X-ray diffraction (XRD) patterns were performed using a Shimadzu XRD-6000 diffractometer (Shimadzu, Kyoto, Japan). A Shimadzu UV-3600 Pharma Spec UV spectrophotometer was used to obtain the UV-Vis absorption spectra. The photoelectric performances were analyzed by a program-controlled semiconductor characterization system (Keithley 2450 Source Meter, Solon, OH, USA). The light source was provided by a 30 W deuterium lamp, and a monochromatic lamp was used to provide monochromatic light.

3. Results and Discussion

The UVA photodetector with the structure of FTO/TiO_2 nanorods array/polycrystalline perovskite $MAPbCl_3$ is shown in Figure 1. TiO_2 nanorods/perovskite $MAPbCl_3$ heterojunctions worked as the active layer. FTO and Ag served as electrodes (A mask plate with a hollow circular pattern (about 0.25 mm^2) was used to mask the material. Silver paste electrodes were coated on the FTO and the material, respectively, and the leads were led out for testing. Then, the whole device was dried at 75 °C for 15 min to stabilize the electrodes. Then, two red and black wires were led out from the Keithley 2450, with the red wire (positive) connected to the Ag above the FTO and the black wire (negative) connected to the Ag above the semiconductor).

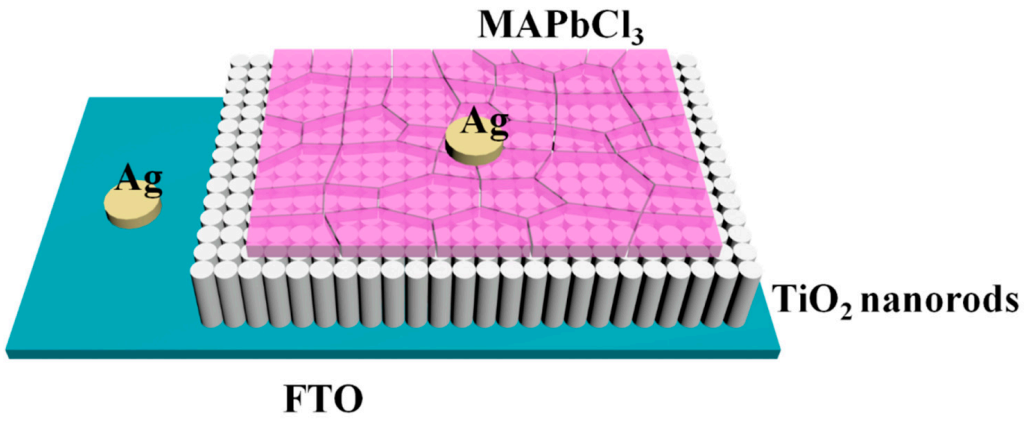

Figure 1. Structure of the TiO_2 nanorods array/$MAPbCl_3$ heterojunction photodetector.

The morphology of TiO_2 one-dimensional nanorods array film on FTO and TiO_2 nanorods/$MAPbCl_3$ heterojunctions on FTO is shown in Figure 2. Figure 2a,b show the top-view and the sectional-view SEM images of the TiO_2 one-dimensional nanorods array, respectively. It can be observed that the TiO_2 nanorods array is uniform, compact and perpendicular to the substrate, which is conducive to the preparation of electronic devices. Figure 2c,d show the top-view and the sectional-view SEM images of the TiO_2 nanorods/$MAPbCl_3$ heterojunctions, respectively. It can be found that the polycrystalline $MAPbCl_3$ film prepared by the one-step method covers the surface of TiO_2 nanorods well. The thickness of $MAPbCl_3$ film is about 0.467 μm, and the thickness of TiO_2 nanorods film is about 2.178 μm. There are lots of grain boundaries in polycrystalline $MAPbCl_3$, which could scatter carriers and thus lead to low mobility. The $MAPbCl_3$ layer adheres to the TiO_2 nanorods array layer, which contributes to the high performance of the detector.

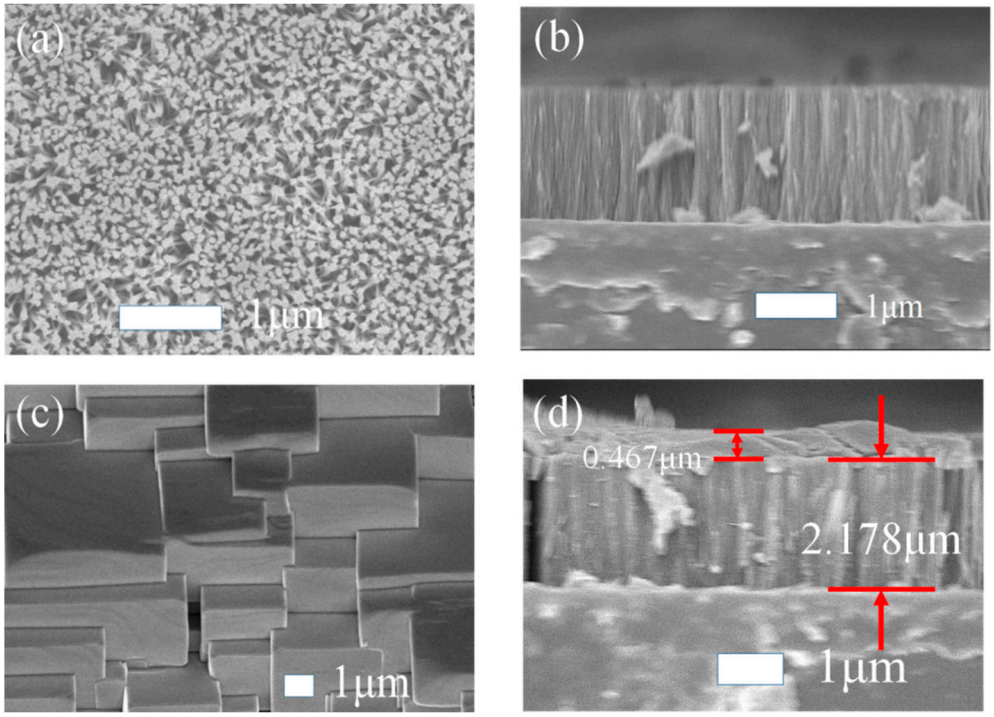

Figure 2. (**a**) Surface SEM image of TiO_2 one-dimensional nanorods array film on FTO. (**b**) Cross-sectional SEM image of TiO_2 one-dimensional nanorods array film on FTO. (**c**) Surface SEM image of TiO_2/$MAPbCl_3$ heterojunction. (**d**) Cross-sectional SEM image of TiO_2/$MAPbCl_3$ heterojunction.

In Figure 3, which displays the XRD patterns of the TiO_2 nanorods array and polycrystalline perovskite $MAPbCl_3$, it can be observed that the crystal diffraction peaks are very high, indicating that the obtained materials have good crystallization and clear crystal particles. Figure 3a shows that the diffraction peaks of the obtained TiO_2 correspond exactly to the peaks of the standard rutile type TiO_2 (JCPDS Card No.76-1938). The characteristic diffraction peaks of $MAPbCl_3$ generated by crystal planes (100), (110), (200), (210) and (211) in Figure 3b are included, indicating that the prepared $MAPbCl_3$ perovskite shows consistency with the previously reported data of $MAPbCl_3$ perovskite obtained through the conventional crystallization technique [31].

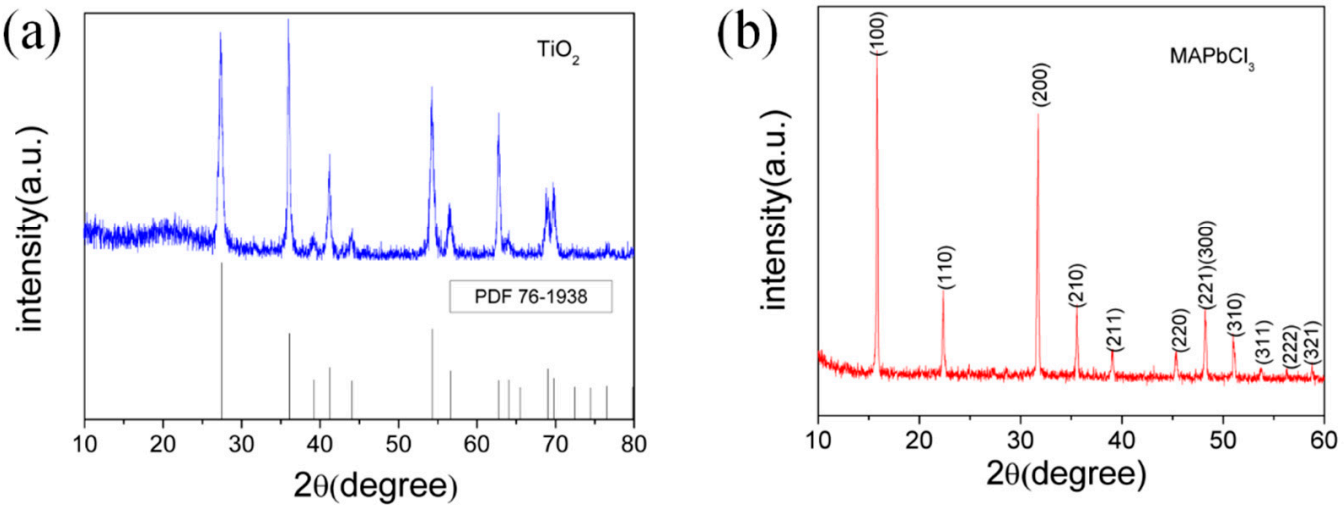

Figure 3. XRD patterns of (**a**) TiO_2 nanorods and (**b**) polycrystalline perovskite $MAPbCl_3$ film.

The optical characteristics of each layer in the photodetector were studied by absorption spectra and Tauc plots, as shown in Figure 4. Figure 4a shows the UV visible absorption spectra of FTO/TiO_2 and FTO/TiO_2/$MAPbCl_3$ from 300 nm to 600 nm. When the photodetector operates, the illumination light enters from the FTO side. Radiation with a wavelength below 300 nm is completely absorbed, and only radiation with a wavelength above 300 nm can pass through the FTO substrate. Moreover, the active layer composed of TiO_2 or TiO_2/$MAPbCl_3$ absorbs radiation with a wavelength below 400 nm. TiO_2 has excellent absorption, from 330 to370 nm, and the absorption decreases over 370 nm, while TiO_2/$MAPbCl_3$ has excellent absorption, from 330 to400 nm, and the absorption decreases over 400 nm. One of the advantages of TiO_2/$MAPbCl_3$ is that it increases the detector's response range closer to 400 nm. Therefore, the radiation whose wavelengths distribute between 300 nm and 400 nm can be collected by TiO_2/$MAPbCl_3$, as shown in the inset of Figure 4b, which corresponds to the UVA range. As calculated in Figure 4b Tauc plots, the bandgap width of rutile TiO_2 is 3.05 eV and the bandgap width becomes 2.98 eV when introducing $MAPbCl_3$.

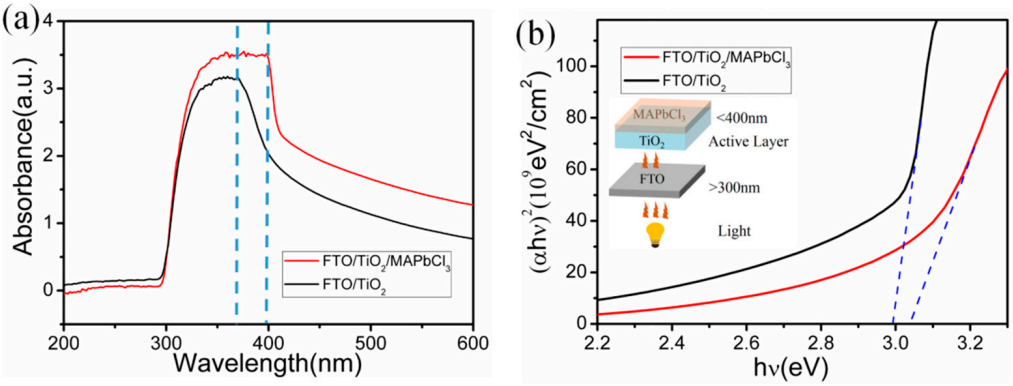

Figure 4. (**a**) UV-visible absorption spectra of FTO/TiO_2 and FTO/TiO_2/$MAPbCl_3$. (**b**) Tauc plots of FTO/TiO_2 and FTO/TiO_2/$MAPbCl_3$. The inset is a schematic diagram of light transmission.

The absorption edge of TiO_2/$MAPbCl_3$ shows a slighter redshift than that of TiO_2, indicating a narrower bandgap of TiO_2/$MAPbCl_3$, which will provide a possibility to adjust the detector's response range. The practical absorption edge of TiO_2 was lower than the theoretical value of pure rutile TiO_2 (1240/3.0 = 413 nm). This may be attributed to the size quantization of nanorods, which has been demonstrated by Brus [32]:

$$\Delta E_g = \frac{\pi^2 h^2}{2R^2}\left(\frac{1}{m_e^*} + \frac{1}{m_h^*}\right) - \frac{1.82e^2}{\varepsilon_R} + \text{polarizaitonterms} \quad (1)$$

where R is the radius of semiconductor particle, m_e^* and m_h^* are effective masses of the electron and hole in the semiconductor, ε_R is the permittivity of rutile TiO_2, h is the Planck constant, ΔE_g is the bandgap difference between the original bulk size and nanoscale of the same semiconductor material. According to this formula, the absorption edge will move to the short wavelength as the particle size decreases [33].

The I–V characteristics of the UV detector based on FTO/TiO_2, FTO/$MAPbCl_3$ and FTO/TiO_2/$MAPbCl_3$ in dark and under illumination are shown in Figure 5. The prepared UV detectors have the characteristics of Schottky diodes, which exhibit nonlinear and unsaturated behavior, as is shown in Figure 5d–f. Under forward bias, the dark current increases rapidly and results in large noise. Therefore, we focus on the reverse characteristics of the detector. For the UV detector based on FTO/TiO_2, at −2 V bias, the dark current is 1.557×10^{-6} A, and the photocurrent reaches 1.359×10^{-4} A under the irradiation of 200 μW/cm^2 at a wavelength of 350 nm UV light, as shown in Figure 5a. For the UV detector based on FTO/$MAPbCl_3$, at −2 V bias, the dark current is 1.043×10^{-9} A, and the photocurrent reaches 1.561×10^{-7} A under the irradiation of 580 μW/cm^2 at a

wavelength of 390 nm UV light, as shown in Figure 5b. For the UV detector based on FTO/TiO_2/$MAPbCl_3$, at −2 V bias, the dark current is 2.69 × 10^{-10} A and the photocurrent reaches 1.632 × 10^{-4} A under the irradiation of 255 μW/cm^2 at a wavelength of 360 nm UV light, as shown in Figure 5c. The ratio of light to dark current is more than six orders of magnitude, which proves that the optical properties of the TiO_2/$MAPbCl_3$ heterojunction detector meet our requirements.

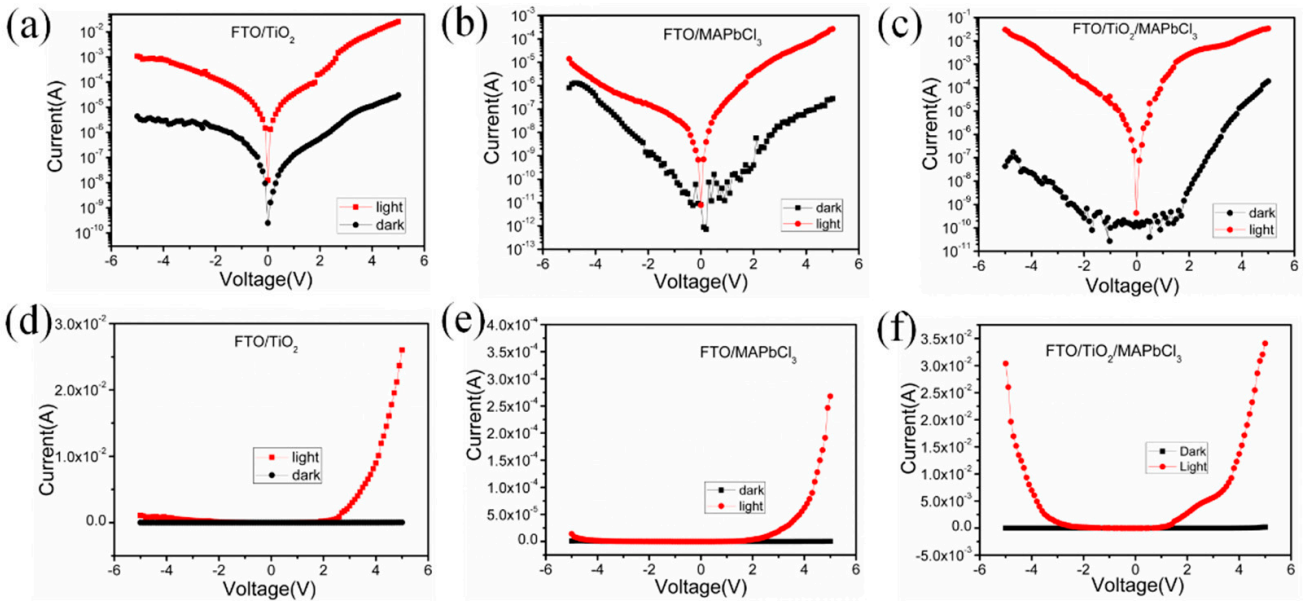

Figure 5. I–V characteristics of the UV detector based on (**a**) FTO/TiO_2, (**b**) FTO/$MAPbCl_3$ and (**c**) FTO/TiO_2/$MAPbCl_3$ in dark and under illumination in logarithmic coordinates; (**d**) FTO/TiO_2, (**e**) FTO/$MAPbCl_3$ and (**f**) FTO/TiO_2/$MAPbCl_3$ in dark and under illumination in linear coordinates.

Figure 6 shows I–V characteristics of FTO/TiO_2/$MAPbCl_3$ UV detector in dark and at a wavelength of 360 nm UV light with various light intensity. All data were obtained at −2 V bias. Under the irradiation of 120 μW/cm^2, the dark current is 3.69 × 10^{-12} A and the photocurrent reaches 3.621 × 10^{-6} A. Under the irradiation of 185 μW/cm^2, the dark current is 2.27 × 10^{-9} A and the photocurrent reaches 1.37 × 10^{-5} A. Under the irradiation of 255 μW/cm^2, the dark current is 2.69 × 10^{-10} A and the photocurrent reaches 1.632 × 10^{-4} A. Under the irradiation of 345 μW/cm^2, the dark current is 1.516 × 10^{-9} A and the photocurrent reaches 2.484 × 10^{-4} A. Compared with dark current of FTO/TiO_2 UV detector, which is 10^{-6} A, the dark current of FTO/TiO_2/$MAPbCl_3$ UV detector improved a lot, which changes from 10^{-9} A to 10^{-12} A. The photo current increased as irradiation increased.

The introduction of TiO_2/$MAPbCl_3$ heterojunction plays an important role in light-to-dark current ratio. The only difference between FTO/TiO_2 and FTO/TiO_2/$MAPbCl_3$ detectors is the TiO_2/$MAPbCl_3$ active layer in the latter. The energy level diagrams and the schematic band diagrams of TiO_2/$MAPbCl_3$ heterojunction are shown in Figure 7a [24,34]. A built-in electric field would be formed at the TiO_2/$MAPbCl_3$ interface [2,35,36]. The TiO_2/$MAPbCl_3$ detector has characteristics similar to Schottky diode. That is, at forward bias, the built-in electric field is weakened and current increases. At reversed bias, the built-in electric field is enhanced and the current reduces. Compared to the TiO_2 detector, the dark current of TiO_2/$MAPbCl_3$ detector was reduced due to the built-in electric field of the heterojunction. Furthermore, the TiO_2/$MAPbCl_3$ contact interface between horizontal $MAPbCl_3$ polycrystalline and vertically aligned TiO_2 nanorods array can produce many localized depletion regions, which contribute to lower dark current. What's more, grain boundaries in polycrystalline $MAPbCl_3$ could scatter carriers in the dark and thus lower mobility. Therefore, the dark current of TiO_2/$MAPbCl_3$ heterojunction UV detector is

much lower than that of pure TiO_2 UV detector. Under illumination, photogenerated electron–hole pairs can be excited in two materials, which are separated by the built-in electric field at the TiO_2/$MAPbCl_3$ interface. Electrons flow along the vertical downward direction of the TiO_2 nanorods, while holes are along the plane direction of the $MAPbCl_3$ film, so it is difficult for recombination and the collection efficiency of carriers improves. Halogen interstitial defects or MA on halogen antisite defects in polycrystalline $MAPbCl_3$ create deep level defects that can trap holes and can be recombination centers affected by the nonequilibrium carriers [37]. Therefore, under illumination, compared with a pure TiO_2 UV detector, TiO_2/$MAPbCl_3$ UV detector produces more photogenerated carriers [38,39].

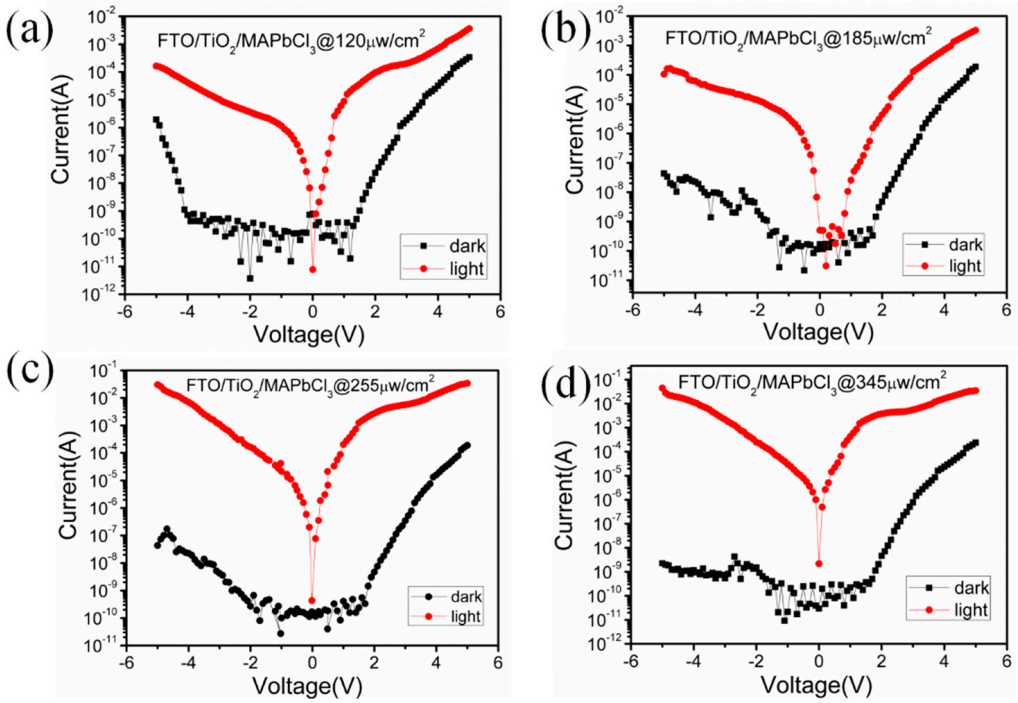

Figure 6. I–V characteristics of TiO_2/$MAPbCl_3$ UV detector in dark and under illumination in logarithmic coordinates with various irradiation (**a**) 120 μW/cm^2, (**b**) 185 μW/cm^2, (**c**) 255 μW/cm^2 and (**d**) 345 μW/cm^2.

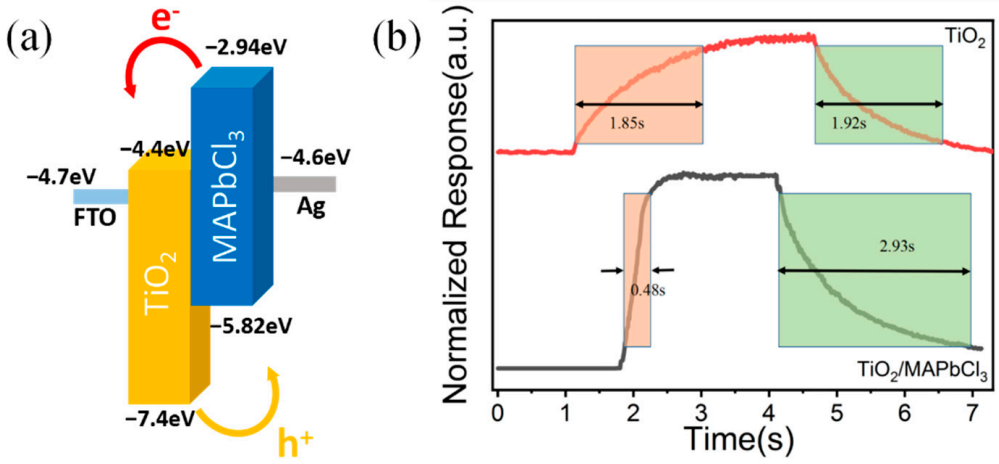

Figure 7. (**a**) The energy level diagrams of TiO_2/$MAPbCl_3$ heterojunction. (**b**) Rise times and decay times of pure TiO_2 detector and TiO_2/$MAPbCl_3$ detector.

Figure 7b displays the response and recovery characteristics of the detectors at −2 V bias, obtained from measuring the voltage variation of a 1 MΩ load resistance in the test circuit. The rise times of the TiO_2 detector and TiO_2/$MAPbCl_3$ detector are 1.85 s and 0.48 s, respectively, and the fall times are 1.92 s and 2.93 s, respectively. The reason why there is an improvement in response characteristic is that the photogenerated electron–hole pairs are rapidly separated by the built-in electric fields of many localized heterojunction regions, as mentioned above. As for the TiO_2/$MAPbCl_3$ photodetector, more photogenerated carriers make the recovery process slower.

Another important parameter for UV photodetector is spectral responsivity and Detectivity* under the irradiation of monochromatic UV light ranging from 310 nm to 450 nm. The spectral responsivity and Detectivity* of both detectors at −2 V bias are shown in Figure 8. The responsivity R was calculated by [32]:

$$\mathrm{R} = \frac{I_p}{A \times E} \tag{2}$$

in which E is the incident optical power, A is the effective photosensitive area of detector and I_p is the photocurrent of the detector under irradiation of the corresponding incident light. The Detectivity* D^*, which demonstrates the ability to detect weak signals from a noise environment, is calculated by [40]:

$$D^* = \frac{R}{(2eI_d/A)^{\frac{1}{2}}} \tag{3}$$

where e is the electronic charge constant, and I_d, which contributes to background noise, is dark current at −2 V bias. Both TiO_2 and TiO_2/$MAPbCl_3$ detectors exhibit well spectrum selectivity for 310~450 nm and R and D^* have increased when compared with the pure TiO_2 device. The response peak of TiO_2/$MAPbCl_3$ detector is 17.25 A/W at 360 nm, and the corresponding D^* is 9.2094 × 10^{11} Jones, which is higher than 15.5 A/W and the corresponding D^* 1.097 × 10^{10} Jones of pure TiO_2 detector at 350 nm, respectively.

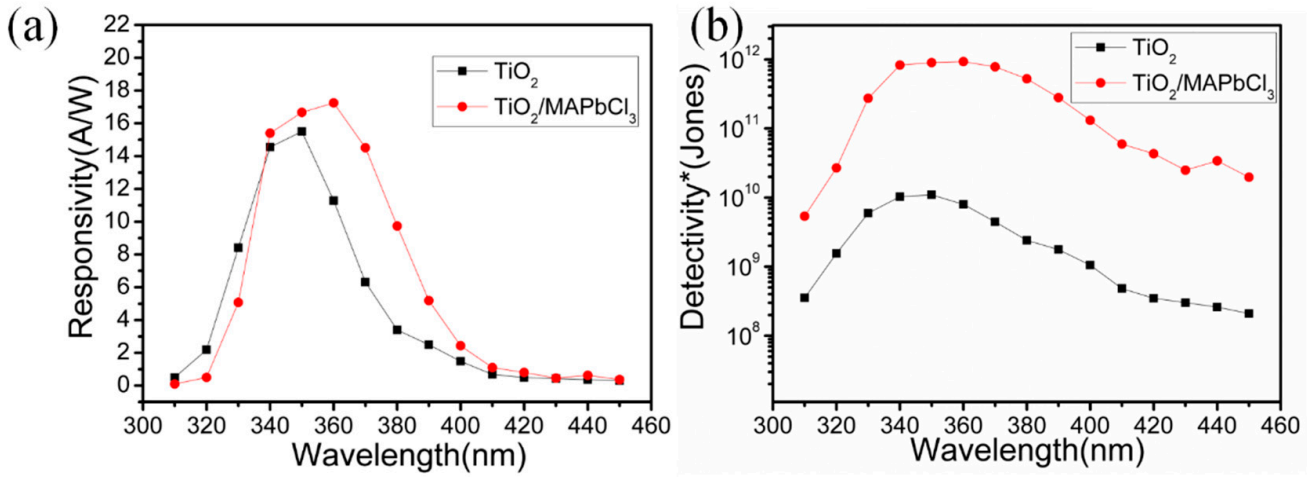

Figure 8. (**a**) The spectral responses of pure TiO_2 and TiO_2/$MAPbCl_3$ heterostructure detectors. (**b**) Spectral Detectivity* of pure TiO_2 and TiO_2/$MAPbCl_3$ heterostructure detectors.

The gain G represents the number of detected charge carriers per single incident photon, and is given by [41]:

$$\mathrm{G} = \frac{I_p/q}{\eta P_{in}/h\upsilon} \tag{4}$$

where η is quantum efficiency and $h\upsilon$ is the excitation energy. Taking TiO_2/$MAPbCl_3$ detector for example, at −2 V bias and at 360 nm UV light, the photocurrent is 1.632 × 10^{-4} A

and the irradiation is 255 $\mu W/cm^2$. The energy of each photon is 1240/360 = 3.44 eV. The incident light energy is $255 \times 0.25 \times 10^{-2} = 0.6375$ μW. The number of photons per second falling on the unit area of the device is $0.6375\ \mu W/(1.602 \times 10^{-19} \times 3.44) = 1.157 \times 10^{12}$. Assuming that all photons are absorbed by the semiconductor surface, the photocurrent generated by these photons is supposed to be $1.157 \times 10^{12} \times 1.602 \times 10^{-19} = 1.853 \times 10^{-7}$ A, so the gain of $TiO_2/MAPbCl_3$ detector is $1.632 \times 10^{-4}/1.853 \times 10^{-7} = 881$. The gain of TiO_2 detector is 963. Both of these detectors have a large gain. Under illumination, the defects of the metal/semiconductor interface will act as minority traps, thus mirroring an equal amount of opposite charges inside the semiconductor and reducing the Schottky barrier height. Therefore, more carriers pass through the barrier and obtain high photocurrent and responsivity, which leads to a large gain. The reason why the gain of $TiO_2/MAPbCl_3$ heterojunction is less than pure TiO_2 is because the detecting wavelength (360 nm) and the corresponding irradiation power (255 $\mu W/cm^2$) of $TiO_2/MAPbCl_3$ is larger than that of TiO_2 (wavelength (350 nm), the corresponding irradiation power (200 $\mu W/cm^2$)). After being calculated according to Formula (4) above, the gain of heterojunction is lower.

The statistical results of the photodetectors' performance parameters are given in Figure 9. The photo and dark currents at −2 V bias of TiO_2 and $TiO_2/MAPbCl_3$ photodetectors are shown in box plots. We have fabricated about eight TiO_2 detectors, and two detectors have good performance like the results above. For example, the ratio of light to dark current at −2 V bias is bigger than two orders of magnitude, and the ratio of others is smaller towards one order of magnitude. The smallest dark current at −2 V bias is close to 10^{-6} A. The reason why the performance of TiO_2 detectors is not stable is due to fabrication process of the devices. In this work, the FTO substrate we used is 1.5 cm × 4 cm so as to be put within the 25 mL autoclave and be faced down. Then TiO_2 nanorods array film can grow on the conductive layer of FTO during a hydrothermal process. Usually, this film covers all the area of the conductive layer, and there are lots of defects in TiO_2 nanorods film, which leads to relatively high dark and photo currents. If the TiO_2 film didn't form well on FTO substrate, the performance of UV detector would be poor.

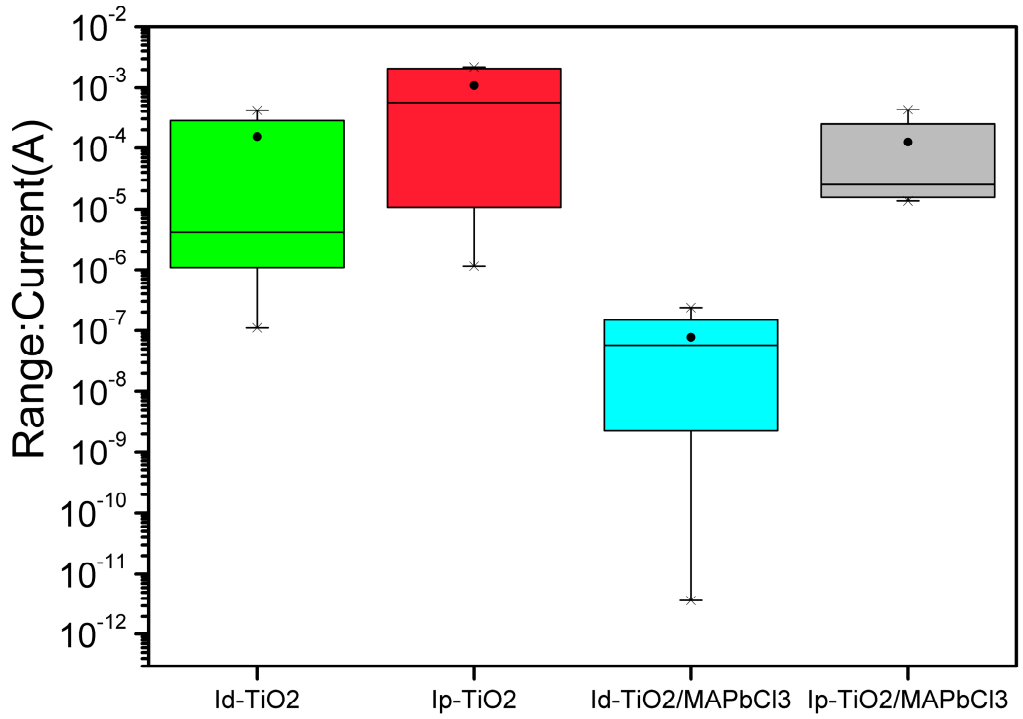

Figure 9. The box plots of the TiO_2 and $TiO_2/MAPbCl_3$ photodetectors' photo and dark currents at reverse 2 V bias.

We have fabricated about fifteen TiO_2/$MAPbCl_3$ detectors and four of them have good performance. That is, the ratio of light to dark current at −2 V bias is bigger than six orders of magnitude, and the ratio of others is smaller from four to two orders of magnitude. The smallest dark current at −2 V bias is close to 10^{-11} A. Because the perovskite $MAPbCl_3$ might not be stable in the atmosphere (H_2O, O_2), and the fabrication process of $MAPbCl_3$ might also influence the quality of film, the performance of TiO_2/$MAPbCl_3$ detectors is not stable compared to our other device with different structures and fabrication procedure (such as MSM detectors with sol-gel method). We have fabricated many detectors and choose the detectors with relatively good performances.

Table 1 lists the dark current and responsive performances comparison between some reported TiO_2 based UV detectors. It is clear that the TiO_2/$MAPbCl_3$-based UV detector shows a high responsivity and detectivity*, a fast response speed and a low dark current.

Table 1. Comparison chart of recent achievements in relation to TiO_2-based UV detectors.

Materials	Fabrication Technique	Dark Current (μA)	Λ (nm)	Responsivity (A/W)	Detectivity* (Jones)	Rise Time (s)	Fall Time (s)	Ref
TiO_2/CuI	nanorods array	4.10×10^{-4} A at 0 V	410	4.5×10^{-3}	1.08×10^{11}	0.33	0.22	[42]
TiO_2/3-BiOCl	nanotube	7.49×10^{-3} A at −5 V	350	7.92	1.42×10^{13}	17.3	1.68	[43]
TiO_2/MoO_3	Sol-gel method	2.856 at −1 V	352	108×10^{-3}	2.26×10^{10}	1.82	1.42	[44]
Ga_2O_3/$MAPbCl_3$	amorphous	6.8 at −1.5 V	398	4.96×10^{-3}	5.4×10^{10}	3.21	0.067	[29]
TiO_2/$MAPbCl_3$	nanorods array	2.69×10^{-4} at −2 V	360	17.25	9.2094×10^{11}	0.48	2.93	This Work

4. Conclusions

A high-performance UVA photodetector based on a polycrystalline perovskite $MAPbCl_3$/TiO_2 nanorods heterojunction has been fabricated successfully. $MAPbCl_3$ polycrystalline perovskite film forms a good heterojunction with TiO_2 one-dimensional nanorods by one-step spin-coating method with antisolvent-assisting. The special structure makes the TiO_2/$MAPbCl_3$ contact interface produce plenty of localized depletion regions. Responsivity and response properties were also improved. Therefore, we successfully improved the performance of pure TiO_2 UV photodetector by introducing a TiO_2/$MAPbCl_3$ heterojunction. These results indicate that the TiO_2/$MAPbCl_3$ heterojunction detector is a potential candidate for UV detection.

Author Contributions: All the authors contributed to the design and development of the experiments, the implementation and the writing of the paper. Specifically, conceptualization, Y.Z. (Yupeng Zhang) and Y.Z. (Yannan Zhai); methodology, Y.Z. (Yupeng Zhang); validation, Y.Z. (Yannan Zhai) and H.Z.; formal analysis, Z.W. and R.X.; investigation, H.Z. and R.X.; resources, Y.Z. (Yongfeng Zhang) and Z.W.; data curation, Y.Z. (Yupeng Zhang) and Y.Z. (Yannan Zhai); writing—original draft preparation, Y.Z. (Yupeng Zhang) and Y.Z. (Yannan Zhai); writing—review and editing, Y.Z. (Yupeng Zhang), S.R. and J.Z.; visualization, H.Z.; supervision, S.R.; project administration, J.Z.; funding acquisition, S.R. and J.Z. All authors have read and agreed to the published version of the manuscript.

Funding: This research was funded by National Natural Science Foundation of China (Grant No. 12073009, 61974055, U21B2061), Jilin Provincial Natural Science Foundation (20230101185JC), Science and technology research project of Jilin Provincial Department of Education (Grant No. JJKH20220769KJ), Natural Science Foundation of Chongqing City (CSTB2022NSCQ-MSX1173).

Institutional Review Board Statement: Not applicable.

Informed Consent Statement: Not applicable.

Data Availability Statement: The data presented in this study are available on request from the corresponding author.

Conflicts of Interest: The authors declare no conflict of interest.

References

1. Xue, H.L.; Kong, X.Z.; Liu, Z.R.; Liu, C.X.; Zhou, J.R.; Chen, W.Y.; Ruan, S.P.; Xu, Q. TiO_2 based metal-semiconductor-metal ultraviolet photodetectors. *Appl. Phys. Lett.* **2007**, *90*, 3. [CrossRef]
2. Zhang, M.; Zhang, H.F.; Lv, K.B.; Chen, W.Y.; Zhou, J.R.; Shen, L.; Ruan, S.P. Ultraviolet photodetector with high internal gain enhanced by $TiO_2/SrTiO_3$ heterojunction. *Opt. Express* **2012**, *20*, 5936–5941. [CrossRef]
3. Gu, X.H.; Zhang, M.; Meng, F.X.; Zhang, X.D.; Chen, Y.; Ruan, S.P. Influences of different interdigital spacing on the performance of UV photodetectors based on ZnO nanofibers. *Appl. Surf. Sci.* **2014**, *307*, 20–23. [CrossRef]
4. Lee, C.T.; Lin, T.S. ZnO-Based Solar Blind Ultraviolet-C Photodetectors Using SiZnO Absorption Layer. *IEEE Photonics Technol. Lett.* **2015**, *27*, 864–866.
5. Zhang, H.F.; Ruan, S.P.; Xie, T.J.; Feng, C.H.; Qu, P.F.; Chen, W.Y.; Dong, W. $Zr_{0.27}Ti_{0.73}O_2$-Based MSM Ultraviolet Detectors with Pt Electrodes. *IEEE Electron. Device Lett.* **2011**, *32*, 653–655. [CrossRef]
6. Wang, W.L.; Zheng, Y.L.; Li, X.C.; Li, Y.; Huang, L.G.; Li, G.Q. High-performance nonpolar a-plane GaN-based metal-semiconductor-metal UV photo-detectors fabricated on $LaAlO_3$ substrates. *J. Mater. Chem. C* **2018**, *6*, 3417–3426. [CrossRef]
7. Cui, S.J.; Mei, Z.X.; Zhang, Y.H.; Liang, H.L.; Du, X.L. Room-Temperature Fabricated Amorphous Ga_2O_3 High-Response-Speed Solar-Blind Photodetector on Rigid and Flexible Substrates. *Adv. Opt. Mater.* **2017**, *5*, 1700454. [CrossRef]
8. Sulaman, M.; Yang, S.Y.; Jiang, Y.R.; Tang, Y.; Zou, B.S. Enhanced performance of solution-processed broadband photodiodes by epitaxially blending $MAPbBr_3$ quantum dots and ternary PbS_xSe_{1-x} quantum dots as the active layer. *Nanotechnology* **2017**, *28*, 505501. [CrossRef]
9. Xu, R.L.; Ruan, S.P.; Zhang, D.Z.; Li, Z.Q.; Yin, B.; Li, K.Z.; Zhou, J.R.; Chen, Y.; Li, C.N. Enhanced performance of ultraviolet photodetector modified by quantum dots with high responsivity and narrow detection region. *J. Alloys Compd.* **2018**, *751*, 117–123. [CrossRef]
10. Jia, J.; Jeon, S.; Jeon, J.; Xu, J.; Song, Y.J.; Cho, J.H.; Lee, B.H.; Song, J.D.; Kim, H.J.; Hwang, E.; et al. Generalized Scheme for High Performing Photodetectors with a p-Type 2D Channel Layer and n-Type Nanoparticles. *Small* **2018**, *14*, 1703065. [CrossRef] [PubMed]
11. Xu, J.Z.; Yang, W.; Chen, H.Y.; Zheng, L.X.; Hu, M.X.; Li, Y.M.; Fang, X.S. Efficiency enhancement of TiO_2 self-powered UV photodetectors using a transparent Ag nanowire electrode. *J. Mater. Chem. C* **2018**, *6*, 3334–3340. [CrossRef]
12. Zheng, Q.H.; Huang, J.; Han, C.X.; Chen, Y.Q. Self-Powered UV-B Photodetector Based on Hybrid Al:MgZnO/PEDOT:PSS Schottky Diode. *IEEE Electron. Device Lett.* **2017**, *38*, 79–82. [CrossRef]
13. Yin, B.; Zhang, H.Q.; Qiu, Y.; Luo, Y.M.; Zhao, Y.; Hu, L.Z. The light-induced pyro-phototronic effect improving a ZnO/NiO/Si heterojunction photodetector for selectively detecting ultraviolet or visible illumination. *Nanoscale* **2017**, *9*, 17199–17206. [CrossRef]
14. Zhang, H.J.; Abdiryim, T.; Jamal, R.; Li, J.X.; Liu, H.L.; Kadir, A.; Zou, D.N.; Che, Y.Z.; Serkjan, N. Self-powered TiO_2 NRs UV photodetectors: Heterojunction with PTTh and enhanced responsivity by Au nanoparticles. *J. Alloys Compd.* **2022**, *899*, 163279. [CrossRef]
15. Xia, W.W.; Qian, H.Y.; Zeng, X.H.; Sun, J.W.; Wang, P.D.; Luo, M.; Dong, J. TiO_2@Sn_3O_4 nanorods vertically aligned on carbon fiber papers for enhanced photoelectrochemical performance. *RSC Adv.* **2019**, *9*, 23334–23342. [CrossRef]
16. Hu, Y.; Hu, G.X.; Zhang, J.J.; Sang, D.D.; Li, Y.K.; Gao, S.Y. Fabrication of ZnO nanorods/CdS quantum dots and its detection performance in UV-Visible waveband. *Chin. Opt.* **2019**, *12*, 1271–1278. [CrossRef]
17. Baghchesara, M.A.; Yousefi, R.; Cheraghizade, M.; Jamali-Sheini, F.; Saaedi, A. Photocurrent application of Zn-doped CdS nanostructures grown by thermal evaporation method. *Ceram. Int.* **2016**, *42*, 1891–1896. [CrossRef]
18. Li, H.O.; Li, Y.; Xiao, G.L.; Gao, X.; Li, Q.; Chen, Y.H.; Fu, T.; Sun, T.Y.; Zhang, F.B.; Yu, N.S. Simple fabrication ZnO/beta-Ga_2O_3 core/shell nanorod arrays and their photoresponse properties. *Opt. Mater. Express* **2018**, *8*, 794–803. [CrossRef]
19. Huang, L.J.; Tian, H.P.; Zhou, J.; Ji, Y.F. Design Low Crosstalk Ring-Slot Array Structure for Label-Free Multiplexed Sensing. *Sensors* **2014**, *14*, 15658–15668. [CrossRef] [PubMed]
20. Liu, Z.C.; Zhao, D.; Min, T.; Wang, J.; Chen, G.Q.; Wang, H.X. Photovoltaic Three-Dimensional Diamond UV Photodetector with Low Dark Current and Fast Response Speed Fabricated by Bottom-Up Method. *IEEE Electron. Device Lett.* **2019**, *40*, 1186–1189. [CrossRef]
21. Karaagac, H.; Aygun, L.E.; Parlak, M.; Ghaffari, M.; Biyikli, N.; Okyay, A.K. Au/TiO_2 nanorod-based Schottky-type UV photodetectors. *Phys. Status Solidi-Rapid Res. Lett.* **2012**, *6*, 442–444. [CrossRef]
22. Liu, Y.C.; Zhang, Y.X.; Yang, Z.; Feng, J.S.; Xu, Z.; Li, Q.X.; Hu, M.X.; Ye, H.C.; Zhang, X.; Liu, M.; et al. Low-temperature-gradient crystallization for multi-inch high-quality perovskite single crystals for record performance photodetectors. *Mater. Today* **2019**, *22*, 67–75. [CrossRef]
23. Jena, A.K.; Kulkarni, A.; Miyasaka, T. Halide Perovskite Photovoltaics: Background, Status, and Future Prospects. *Chem. Rev.* **2019**, *119*, 3036–3103. [CrossRef] [PubMed]
24. Maculan, G.; Sheikh, A.D.; Abdelhady, A.L.; Saidaminov, M.I.; Hague, M.A.; Murali, B.; Alarousu, E.; Mohammed, O.F.; Wu, T.; Bakr, O.M. $CH_3NH_3PbCl_3$ Single Crystals: Inverse Temperature Crystallization and Visible-Blind UV-Photodetector. *J. Phys. Chem. Lett.* **2015**, *6*, 3781–3786. [CrossRef] [PubMed]
25. Ding, J.; Yan, Q.F. Progress in organic-inorganic hybrid halide perovskite single crystal: Growth techniques and applications. *Sci. China Mater.* **2017**, *60*, 1063–1078. [CrossRef]

26. Parandin, F.; Heidari, F.; Aslinezhad, M.; Parandin, M.M.; Roshani, S.; Roshani, S. Design of 2D photonic crystal biosensor to detect blood components. *Opt. Quantum Electron.* **2022**, *54*, 618. [CrossRef]
27. Wang, X.D.; Li, W.G.; Liao, J.F.; Kuang, D.B. Recent Advances in Halide Perovskite Single-Crystal Thin Films: Fabrication Methods and Optoelectronic Applications. *Solar RRL* **2019**, *3*, 1800294. [CrossRef]
28. Yang, J.L.; Liu, K.W.; Cheng, Z.; Jing, P.T.; Ai, Q.; Chen, X.; Li, B.H.; Zhang, Z.Z.; Zhang, L.G.; Zhao, H.F.; et al. Investigation of Interface Effect on the Performance of $CH_3NH_3PbCl_3$/ZnO UV Photodetectors. *ACS Appl. Mater. Interfaces* **2018**, *10*, 34744–34750. [CrossRef] [PubMed]
29. Liu, S.; Jiao, S.J.; Lu, H.L.; Nie, Y.Y.; Gao, S.Y.; Wang, D.B.; Wang, J.Z.; Zhao, L.C. Polycrystalline perovskite $CH_3NH_3PbCl_3$/amorphous Ga_2O_3 hybrid structure for high-speed, low-dark current and self-powered UVA photodetector. *J. Alloys Compd.* **2022**, *890*, 161827. [CrossRef]
30. Zhang, H.F.; Li, H.L.; Zhang, M.; Feng, C.H.; Gu, X.H.; Xu, Y.; Zhou, J.R.; Ruan, S.P. Photovoltaic ultraviolet detectors based on $Zr_{0.04}Ti_{0.96}O_2$ solid solution nanowire arrays. *Appl. Opt.* **2013**, *52*, 750–754. [CrossRef] [PubMed]
31. Baikie, T.; Barrow, N.S.; Fang, Y.A.; Keenan, P.J.; Slater, P.R.; Piltz, R.O.; Gutmann, M.; Mhaisalkar, S.G.; White, T.J. A combined single crystal neutron/X-ray diffraction and solid-state nuclear magnetic resonance study of the hybrid perovskites $CH_3NH_3PbX_3$ (X = I, Br and Cl). *J. Mater. Chem. A* **2015**, *3*, 9298–9307. [CrossRef]
32. Kong, X.Z.; Liu, C.X.; Dong, W.; Zhang, X.D.; Tao, C.; Shen, L.; Zhou, J.R.; Fei, Y.F.; Ruan, S.P. Metal-semiconductor-metal TiO_2 ultraviolet detectors with Ni electrodes. *Appl. Phys. Lett.* **2009**, *94*, 123502. [CrossRef]
33. Zhang, H.F.; Feng, C.H.; Liu, C.X.; Xie, T.J.; Zhou, J.R.; Ruan, S.P. $Zr_xTi_{1-x}O_2$-Based Ultraviolet Detectors Series. *IEEE Electron. Device Lett.* **2011**, *32*, 934–936. [CrossRef]
34. Yin, B.; Zhang, Y.F.; Li, K.Z.; Zhou, J.R.; Liu, C.X.; Zhang, M.; Ruan, S.P. UV detector based on an FTO/TiO_2/MoO_3 heterojunction with a potential well trapping electrons in the dark. *Nanotechnology* **2019**, *30*, 465501. [CrossRef] [PubMed]
35. Zhang, H.F.; Ruan, S.P.; Feng, C.H.; Xu, B.K.; Chen, W.Y.; Dong, W. Photoelectric Properties of TiO_2-ZrO_2 Thin Films Prepared by Sol-Gel Method. *J. Nanosci. Nanotechnol.* **2011**, *11*, 10003–10006. [CrossRef] [PubMed]
36. Lv, K.B.; Zhang, M.; Liu, C.X.; Liu, G.H.; Li, H.C.; Wen, S.P.; Chen, Y.; Ruan, S.P. TiO_2 ultraviolet detector based on $LaAlO_3$ substrate with low dark current. *J. Alloys Compd.* **2013**, *580*, 614–617. [CrossRef]
37. Jung, H.R.; Cho, Y.; Jo, W. UV and Visible Photodetectors of $MAPbBr_3$ and $MAPbCl_3$ Perovskite Single Crystals via Single Photocarrier Transport Design. *Adv. Opt. Mater.* **2022**, *10*, 2102175. [CrossRef]
38. Zhao, Y.; Li, C.L.; Shen, L. Recent research process on perovskite photodetectors: A review for photodetector—Materials, physics, and applications. *Chin. Phys. B* **2018**, *27*, 127806. [CrossRef]
39. Zhang, D.Z.; Liu, C.Y.; Li, K.Z.; Ruan, S.P.; Zhou, J.R.; Zhang, X.D.; Chen, Y. Modulated charge transport characteristics in solution-processed UV photodetector by incorporating localized built-in electric field. *J. Alloys Compd.* **2019**, *774*, 887–895. [CrossRef]
40. Liu, X.; Gu, L.L.; Zhang, Q.P.; Wu, J.Y.; Long, Y.Z.; Fan, Z.Y. All-printable band-edge modulated ZnO nanowire photodetectors with ultra-high detectivity. *Nat. Commun.* **2014**, *5*, 4007. [CrossRef]
41. Wang, F.; Wang, Z.; Yin, L.; Cheng, R.; Wang, J.; Wen, Y.; Shifa, T.A.; Wang, F.; Zhang, Y.; Zhan, X.; et al. 2D library beyond graphene and transition metal dichalcogenides: A focus on photodetection. *Chem. Soc. Rev.* **2018**, *47*, 6296–6341. [CrossRef] [PubMed]
42. Zhou, Z.Y.; Li, X.X.; Zhao, F.Z.; Wang, C.; Zhang, M.L.; He, S.L.; Zhang, Y.Q.; Zhang, D.Y.; Xu, M.; Zhang, L.C. Self-powered heterojunction photodetector based on thermal evaporated p-CuI and hydrothermal synthesised n-TiO_2 nanorods. *Opt. Mater. Express* **2022**, *12*, 392–402. [CrossRef]
43. Ouyang, W.X.; Teng, F.; Fang, X.S. High Performance BiOCl Nanosheets/TiO_2 Nanotube Arrays Heterojunction UV Photodetector: The Influences of Self-Induced Inner Electric Fields in the BiOCl Nanosheets. *Adv. Funct. Mater.* **2018**, *28*, 1707178. [CrossRef]
44. Ezhilmaran, B.; Dhanasekar, M.; Bhat, S.V. Solution processed transparent anatase TiO_2 nanoparticles/MoO_3 nanostructures heterojunction: High performance self-powered UV detector for low-power and low-light applications. *Nanoscale Adv.* **2021**, *3*, 1047–1056. [CrossRef] [PubMed]